Ceramics International 50 (2024) 37779–37789

Contents lists available at ScienceDirect

Ceramics International

journal homepage: www.elsevier.com/locate/ceramint

In vitro biocompatibility and stem cell regenerative assessment of hollow hydroxyapatite spheres deposited wollastonite/$Ca_2P_6O_{17}$/TCP/doped-wollastonite scaffolds

Lakshmi Jeevithan [a,1], Paula M. Riosalido [b,1], Ángel Murciano [c], Pablo Velásquez [b], Piedad N. De Aza [b], Jeevithan Elango [a,d,e], Wenhui Wu [a,**], Jose Eduardo Mate Sanchez de Val [d,*]

[a] Department of Marine Biopharmacology, College of Food Science and Technology, Shanghai Ocean University, Shanghai, 201306, China
[b] Instituto de Bioingeniería, Universidad Miguel Hernández, Avda. Ferrocarril s/n, Elche, Alicante, 03202, Spain
[c] Departamento de Materiales, Óptica y Tecnología Electrónica, Universidad Miguel Hernández, Avda. Universidad s/n, Elche, Alicante, 03202, Spain
[d] Department of Biomaterials Engineering, Faculty of Health Sciences, UCAM Universidad Católica San Antonio de Murcia, Guadalupe, 30107, Murcia, Spain
[e] Center of Molecular Medicine and Diagnostics (COMManD), Department of Biochemistry, Saveetha Dental College and Hospitals, Saveetha Institute of Medical and Technical Sciences (SIMATS), Saveetha University, Chennai, 600 077, India

ARTICLE INFO

Handling Editor: Dr P. Vincenzini

Keywords:
Multilayer scaffolds
Hydroxyapatite hollow spheres
Biocompatibility
Fibroblasts
Mesenchymal stem cells

ABSTRACT

This research examines the biological behavior of multilayer ceramic-glass scaffolds for bone tissue engineering. The scaffolds consist of a high-strength core of wollastonite and P6 ($Ca_2P_6O_{17}$), with a sequential coating of TCP and wollastonite doped with Na^+, K^+ and Mg^{2+} ions to confer bioactivity to the system. Two formulations were investigated: a magnesium-deficient one, which served as a microstructure control, and a magnesium-rich one in which hollow hydroxyapatite (HA) spheres precipitated after one week of immersion in simulated body fluid (SBF). These formulations are denoted as C-Scaffold and HA-Scaffold, respectively. Further exploration and comparison of the physiological effects of both scaffolds is necessary to fully understand their potential as drug release agents and associated therapeutic advantages. The study considered aspects such as protein adhesion, cell morphology, and the inflammatory response. The results showed that the HA-Scaffold had over 34 % more plasma protein adhesion compared to the C-Scaffold. Similarly, cell proliferation assays showed increased cell growth in both HFF-1 fibroblasts and mesenchymal stem cells (MSCs) treated with HA-Scaffold compared to C-Scaffold. This may be attributed to the higher protein adsorption, which acts as a facilitator for cell adhesion. Three-dimensional photography from computerized microtomography confirmed that the scaffolds have a similar morphology and porosity to the intricate structure of trabecular bone in the humeral head. The study shows that the scaffolds made of Wollastonite/$Ca_2P_6O_{17}$/TCP/Doped-Wollastonite with HA hollow spheres are highly suitable for use in this bone segment due to their overall porosity of over 86 % and approximate mechanical strength of 1.6 MPa. These findings demonstrate the biocompatibility and enhanced biological properties of the scaffolds, making them an excellent material for bone tissue engineering.

1. Introduction

The world population, characterized by constant aging, is facing a significant increase in the frequency of bone defects [1–3]. This phenomenon is reflected in concerning statistics, highlighting the urgent need to address these conditions effectively. While bone transplantation remains the gold standard for treating skeletal defects, it is burdened by substantial drawbacks, encompassing high costs and associated risks such as inflammation, neurovascular damage, immune rejection, or inadequate osseointegration [4–7].

The limitations of current therapeutic options drive research efforts toward more effective and innovative solutions. In this context, bone

* Corresponding author.
** Corresponding author.
E-mail addresses: lakshmijeevithan@gmail.com (L. Jeevithan), priosalido@umh.es (P.M. Riosalido), amurciano@umh.es (Á. Murciano), pavelasquez@umh.es (P. Velásquez), piedad@umh.es (P.N. De Aza), jelango@ucam.edu (J. Elango), whwu@shou.edu.cn (W. Wu), jemate@ucam.edu (J.E. Mate Sanchez de Val).
[1] These authors contributed equally.

https://doi.org/10.1016/j.ceramint.2024.07.141
Received 26 March 2024; Received in revised form 25 June 2024; Accepted 11 July 2024
Available online 14 July 2024

tissue engineering arises to overcome the inherent challenges in osseous regeneration by formulating artificial, functional structures that exhibit properties and an architecture resembling those of native bone [3,7,8]. In this regard, the careful choice of both the material and the fabrication method is critical [7,8]. Among the various methodologies available, the Sol-Gel approach stands out as an essential tool, distinguished by its versatility and ability to generate scaffolds with specific properties [9–11]. This method offers the possibility of integrating different materials into a single structure through the deposition of various coatings, resulting in the formation of multilayer scaffolds.

The strategic choice of these materials seeks to provide beneficial and essential functions to stimulate and direct bone regeneration, highlighting properties such as mechanical strength, crucial in osseous defects affecting bone under load, as well as biocompatibility, bioactivity and osteoinduction.

The multilayer scaffolds under study are comprised, progressively from the core outwards, of wollastonite, the glassy phase known as P6 ($Ca_2P_6O_{17}$), tricalcium phosphate (TCP) and, as the surface phase, wollastonite doped with Na^+, K^+ and Mg^{2+} ions. The combination of the properties of P6 as a cohesive agent, TCP as a source of Ca and P, and the bioactivity of wollastonite, together with the ion doping strategy, makes these scaffolds a promising clinical alternative to current treatments. Our recent study reported the fabrication of alumina based-wollastonite multilayer porous scaffolds for bone tissue engineering [12]. Earlier studies also attempted to investigate the bone regenerative ability of multilayer wollastonite scaffolds combined with TCP [13,14], fibrin [15], poly(lactic acid) [16], Zn and Mg doping [17], poly(L-lactide)/apatite [18], and chitosan/apatite [19]. Furthermore, previous studies have outlined that, upon immersing these scaffolds in simulated body fluid (SBF), hollow spheres of hydroxyapatite (HA) precipitate, revealing their potential as agents for controlled drug release [20–22]. Given the associated advantageous prospects, this study investigated the interaction of these scaffolds with biological systems, aiming to predict their *in vivo* response.

2. Materials and methods

2.1. Fabrication of multilayer scaffolds

The multilayer scaffolds were fabricated using the Sol-Gel method along with the polymer sponge replication technique. A 20 ppi polyurethane sponge served as a template for depositing the different materials that comprise the scaffolds, selecting the indicated porosity of the polyurethane sponge in order to obtain a final open porosity within the range 50–300 μm. The wollastonite internal layer was formed by combining 19.28 mL of Tetraethyl Orthosilicate (TEOS, Aldrich 98 %), 8.62 g of calcium carbonate ($CaCO_3$, Sigma ≥99 %), 5 mL of ethanol, 20 mL of distilled water, and 1 mL of hydrochloric acid (HCl 37 %, Ensure). After sintering, the polymer sponge was replaced by wollastonite, which served as the new ceramic template for the following layers.

Next, a layer containing the vitreous phase P6 was added to the scaffold in order to enhance the mechanical strength and tackle the brittleness of the wollastonite core. The composition was created by mixing 18.46 mL of Triethyl Phosphate (TEP, Aldrich ≥99.8 %), 3.72 g of $CaCO_3$, 1 g of lithium carbonate (Li_2CO_3, Sigma-Aldrich ≥99 %), 5 mL of ethanol, 20 mL of distilled water, and 2 mL of HCl 37 %. The excess glassy phase was removed from the core through a chemical attack process using an etching solution called TRIS. To create this solution, 7.6 g of tris(hydroxymethyl)aminomethane ($NH_2C(CH_2OH)_3$, Sigma Aldrich ≥99.8 %); and 1.168 g of calcium chloride ($CaCl_2$, Riedel-de Haën ≥97 %) were diluted in distilled water and HCl to a final volume of 1 L. The pH was finally adjusted to a value ranging from 7.3 to 7.4. The cores were then immersed in 50 mL of the solution and maintained at 50 °C for 24 h. The subsequent step involved the application of a third layer, comprising TCP, which served as a source of calcium and phosphate ions to facilitate HA deposition. The layer was formed through a chemical reaction involving 10.965 mL of TEP, 9.68 g of $CaCO_3$, 5 mL of ethanol, 20 mL of distilled water, and 2 mL of 37 % HCl.

Finally, wollastonite was once again chosen as the surface layer. The layer was formulated as described above, with the addition of 0.5 g sodium carbonate (Na_2CO_3, Sigma ≥99 %), 0.5 g of potassium carbonate (K_2CO_3, Sigma ≥99 %) (C-Scaffold), and an additional 0.5 g of magnesium carbonate ($MgCO_3$, Sigma Aldrich ≥99 %) (HA-Scaffold). It is worth noting that the pH of all syntheses was adjusted to a value of 2–3. After applying sufficient layers of each material, the sample underwent a sintering process. The temperature was gradually increased from room temperature to 1050 °C, with a holding time of 8 h, and finally cooled to room temperature. The heating rate for the initial layer was approximately 0.32 °C/min, while it was significantly accelerated up to 2 °C/min for the subsequent layers.

To enhance the bio-functional properties, the hollow HA spheres were precipitated on the HA-Scaffold after 7 days of immersion in simulated body fluid (SBF) and were sustained for an additional 7 days during *in vitro* bioactivity tests (ISO 23317). Subsequently, HA-Scaffold samples were immersed in Falcon tubes containing 50 mL of SBF and incubated for 7 days in a shaking water bath set to physiological temperature (37 ± 0.5 °C). Therefore, the C-Scaffold, which lacks Mg^{2+} and HA, was used as the control scaffold. Table 1 shows the molar percentages of both specimens.

Table 1
The molar fraction of the studied scaffolds.

Component	Molar fraction	
	C-Scaffold	HA-Scaffold
SiO_2	0.248	0.244
CaO	0.494	0.494
P_2O_5	0.207	0.204
Li_2O	0.039	0.038
Na_2O	0.007	0.007
K_2O	0.005	0.005
MgO	–	0.008

2.2. Characterization

2.2.1. Mineralogical characterization

Once the two types of scaffolds were obtained, the mineralogical characterization was carried out by X-ray diffraction (XRD). A Bruker-AXR D8 Advance automated diffractometer using Cu-Kα radiation (1.54056 Å) was used. The Bragg-Brentano theta-2thetha (θ/2θ) geometry was employed to collect the experimental data between 15° and 40° (2θ) at 0.05 steps, and a scanning speed of 5 s. The experimental data was analyzed with the Power Diffraction Match! version 3.16 Build 288 software. The thermal degradation profile of the fabricated scaffold was done by thermogravimetric analysis (TG, Japan Hitachi STA200) in a nitrogen atmosphere with a temperature ranging from 35 to 1100 °C.

2.2.2. Macro and microstructure characterization

The macrostructure of the scaffolds was analyzed using a Nikon SMZ1500 stereomicroscope equipped with a Nikon DXM1200F digital camera. Additionally, the microstructure of the scaffolds was investigated through Field Emission Scanning Electron Microscopy (FESEM) using a ZEISS Sigma 300 VP instrument, coupled with Energy-dispersive X-ray spectroscopy (EDX) from ZEISS SmartEDX. The scanning resolution was set to 5 kV. To improve electrical conductivity and acquire more precise images and spectral data, the samples were metalized with palladium before electron microscopy.

2.2.3. Physical characterization

Given the importance of scaffold porosity, a study of this feature was carried out using the mercury porosimetry technique. A Poromaster 60 GT (Quantachrome Instruments) was used, which worked with a

pressure between 6.393 KPa and 242,995.531 KPa. Pycnometric analysis was also used to determine the macroporosity of the sample. These data were supplemented with the mechanical strength of samples. A compression test was conducted using a Simple Manual Test Stand (SVL-1000 N, IMADA) where samples were subjected to increasing values of manually applied pressure until the sample breakage occurred.

2.3. Effect of scaffolds in plasma protein adhesion

In order to determine the plasma protein adhesion, both the C-Scaffold and HA-scaffolds were incubated in Fetal Bovine Serum (FBS) at 37 °C for 4 h. Then, the FBS was removed, and the scaffolds were washed with Phosphate Buffer Saline (PBS) gently twice, followed by staining with Coomassie Brilliant blue (CBB) G-250 for 2 h at 37 °C. The excess stain was washed out with a destaining solution containing a methanol-water-acetic acid mixture overnight. The FBS untreated scaffolds (Blank) were also stained with CBB G-250. The amount of protein absorbed on the scaffold was determined by measuring the optical density of the supernatant at 590 nm as per our previous method [23].

2.4. Cell culture

The Mesenchymal Stem Cells (MSC) from human bone marrow (CTCC-113-HUM) and Human Foreskin Fibroblasts (HFF-1) (CTCC-001-0346) were purchased from Zhejiang Matson Cell Technology Co., Ltd. (MeisenCTCC), Shanghai, China). The cells were cultured as per the seller's recommendations. Briefly, the MSC cells were cultured in mesenchymal stem cell growth medium (Cat No: CTCC-S019-HUM-M, Lot No: M23SF2204) without FBS and HFF-1 cells were cultured in Dulbecco's Modified Eagle Medium (DMEM) medium containing 15 % FBS with 1 % antibiotics (Penicillin and Streptomycin). The cells were cultured in a standard way until 80 % confluence and then sub-cultured. The cells from passages 3–8 were used for the following experiments. Samples (C-Scaffold and HA-Scaffold) were UV-sterilized for 30 min before cell culture use. The sterilized samples were briefly washed with PBS and equilibrated with respective culture mediums for cell culture.

2.5. Effect of the scaffold on MSC proliferation

The effect of both the C-Scaffold and HA-Scaffold on the proliferation of MSCs was determined as per the previous method [24]. Briefly, the MSCs with a cell density of 5×10^5 seeded on scaffolds in 48 well plates were cultured with a mesenchymal stem cell growth medium.

In parallel, the cells were cultured with Scaffold Conditioned Medium (SCM). The SCM was prepared by incubating scaffolds in mesenchymal stem cell growth medium for 24 h and collected by centrifuge at 2000 g for 5 min. The cells without scaffold or SCM were considered as controls. Both scaffold-seeded and SCM-treated cells were cultured for 3 days and 7 days. After the treatment, the cells were briefly washed with PBS prior to the cck-8 experiment. The proliferation rate of cells was determined by culturing the cells with basal culture medium containing cck-8 reagent for 2 h and measured at 450 nm.

2.6. Biocompatibility

The biocompatibility of both the C-Scaffold and HA-Scaffold was investigated by using HFF-1 cells. Briefly, the HFF-1 cells with a cell density of 1×10^6 per well in 48 well plates, were seeded on both the C-Scaffold and HA-Scaffold and were cultured with DMEM medium containing 15 % FBS for 3 days and 7 days. The compatibility of scaffolds on HFF-1 cells was investigated by the cck-8 method following the previous method. The cells cultured without scaffolds were considered as control.

2.7. Effect of the scaffolds in inflammatory response

To further confirm the biocompatibility, the cellular inflammatory response was measured after treating cells with scaffolds. The MSCs and HFF-1 cells with a cell density of 5×10^5 per well in 98 well plates were seeded on scaffolds and cultured with mesenchymal stem cell growth medium and DMEM medium, respectively, for 3 days and 7 days. After treatment, the cell supernatant was collected after centrifuge at 2000 g for 5 min, and stored at −20 °C until use. The level of cellular cytokines was determined by using IL-2 and IL-6 ELISA kits. The quantitative measurement of IL-2 and IL-6 was determined by following the manufacturer's instructions. The reference standard curves for IL-2 with gradient concentrations (0, 20 pg, 40 pg, 80 pg, 160 pg and 320 pg) and for IL-6 with gradient concentrations (0, 10 pg, 20 pg, 40 pg, 80 pg and160 pg) were plotted (Supplementary Fig. S1 and Fig. S2) for measuring the test sample concentrations.

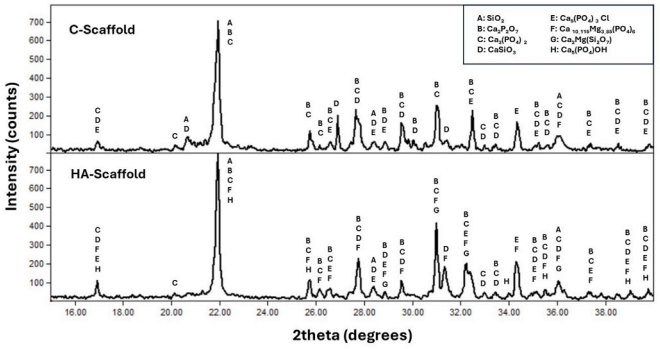

Fig. 1. XRD diffraction patterns of the C-Scaffold (A) and HA-Scaffold (B).

2.8. Effect of the scaffolds on cell morphology

Changes in the morphological features of MSC and HFF-1 after being cultured on scaffolds were determined by SEM [Oxford Xplore, ZEISS GeminiSEM 300]. For this purpose, the MSCs and HFF-1 cells with a cell density of 1×10^6 per well in 24 well plates were cultured on both the C-Scaffold and HA-Scaffold with respective culture media for 3 days and 7 days. After cell culture, the cells on scaffolds were washed with PBS and fixed with 2.5 % glutaraldehyde for 30 min and 4 % formaldehyde for 30 min. After fixation, the scaffold samples with cells were dehydrated with gradient alcohol concentrations (0, 25 %, 50 %, 75 % and 100 % ethanol in PBS) for 10 min each. The dehydrated scaffold cells were air-dried overnight in a sterile biosafety cabinet. Then, scaffold cells were sputter-coated with gold and images were captured by SEM at different magnifications with 15 kV resolution.

2.9. Osteogenic differentiation

The ability of scaffolds in stem cell regeneration was further confirmed by osteogenic differentiation of MSCs culturing with scaffold condition medium. In brief, the MSCs (1×10^6/well) were seeded in 24 well plates and cultured for 21 days with osteogenic medium containing supplements (Shanghai QiDa Biotechnology Co., Ltd, Lot No: P1301) along with scaffold conditioned medium. Osteogenic differentiation was confirmed by standard osteogenic staining methods using alizarin red and von Kossa stains for calcium deposition, and alkaline phosphatase stain.

2.10. Statistical analysis

All the experiments were conducted with triplicate samples, and a concordant value was obtained from these experiments. The values were expressed as means ± SD unless otherwise indicated. The statistical difference and comparisons were made using one-way ANOVA analysis and a p-value less than 0.05 was noted as statistical significance after treating the data in GraphPad Prism 9.4.0 software.

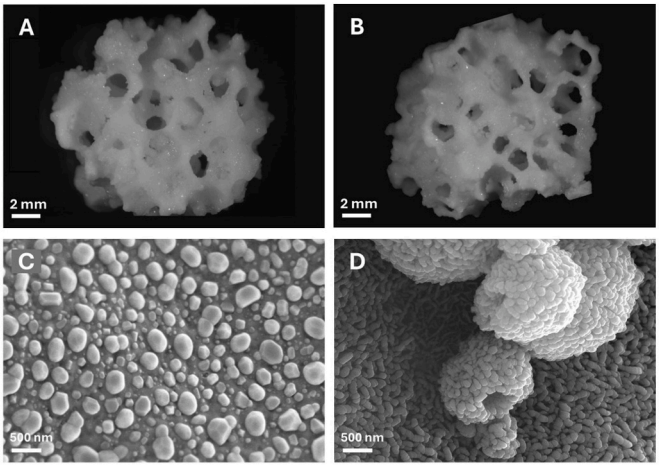

Fig. 2. Structural study of multilayer scaffolds. Optical images of the macrostructure in the top (A) and front view (B), together with FESEM-EDX images of the microstructure of the C-Scaffold (C) and HA-Scaffold (D).

3. Results and discussion

3.1. Mineralogical characterization

As for the mineralogical examination, Fig. 1 shows the XRD spectra of C-Scaffold (Fig. 1A) and HA-Scaffold (Fig. 1B). The XRD spectra confirmed the presence of three layers in both C-Scaffold and HA-Scaffold, and several phases were identified in both scaffolds. These phases were cristobalite (A) (COD 96-900-8225), calcium diphosphate (B) (COD 96-100-1557), TCP (C) (COD 96-151-7239), wollastonite (D) (COD 96-900-5779), and chlorapatite (E) (COD 96-210-5266). In addition, the HA-Scaffold also exhibited magnesium-rich compounds, namely whitlockite, with $Ca_{10.115}\ Mg_{3.85}PO_4$ formula, (F) (COD 96-901-2137) and akermanite, $Ca_2MgSi_2O_7$, (G) (COD 96-900-6942), as well as HA (H) (COD 96-901-4314).

Considering that ionic conductivity is directly proportional to temperature, ionic migration is expected to increase during sintering [25]. This would explain the formation of cristobalite and calcium pyrophosphate (from $CaSiO_3$ and $Ca_2P_6O_{17}$) and whitlockite (from $CaSiO_3$–Na^+, K^+, Mg^{2+} and TCP). However, the chlorapatites was likely formed due to the HCl used in the synthesis process.

The presence of HA peak in the HA-Scaffold confirmed the successful deposition of HA during SBF incubation and the bioactivity of the sample. HA ($Ca_{10}(PO_4)_6(OH)_2$) is the primary inorganic component of human bone [3,7] and is commercially used in bone implants due to its good biocompatibility and ability to integrate seamlessly with natural bone tissue [3,26–28].

3.2. Microstructure

The scaffolds exhibited a macrostructure with open porosity and interconnected porosity, as shown in Fig. 2A and B. As for the microstructure, the surface of the C-Scaffold (Fig. 2C) showed a regular pattern consisting of circular structures mainly composed of calcium and silicon, with a Ca/Si ratio of 0.5 ± 0.07, suggesting the presence of calcium disilicide ($CaSi_2$). Silicates are thought to play an important role in promoting bone matrix formation, given their ability to form a surface HA layer, activated by the dissolution of calcium and silicate ions [29,30].

Upon scanning the HA-Scaffold, their surface was completely covered by a dense, and elongated precipitate (Fig. 2D). This precipitate was rich in calcium and phosphorus at a ratio of 1.62 ± 0.07, which is very similar to the stoichiometric HA Ca/P ratio of 1.67. Additionally, hollow spheres formed by the same elongated structures with a Ca/P ratio of 1.69 ± 0.11 were observed on this deposit. The precipitation of HA can be attributed to the silicate outer layer of the scaffold. This layer promotes the formation of a HA layer through ionic exchange reactions, as described by Hench [31]. Also, this HA layer is capable of binding to bone and a potentially a pro-osteoinductive factor [29]. The morphology of the hollow HA spheres is controlled by the magnesium concentration, while the amount of HA spheres precipitated is controlled by the days of immersion in SBF. Only with seven days of soaking in SBF hollow HA spheres are deposited.

3.3. Physical characterization

As for the physical characterization, the Hg porosimetry technique was used to evaluate the microporosity (<300 μm) of both the C-Scaffold and the HA-Scaffold. The C-Scaffold presented a total porosity of 26.61 %, of which 19.22 % was attributed to interparticle porosity, with a diameter range of 121 - 5.21 μm. The remaining 7.39 % corresponded to intraparticle porosity, characterized by smaller pores with diameters ranging from 0.342 to 0.018 μm. In comparison, the HA-Scaffold

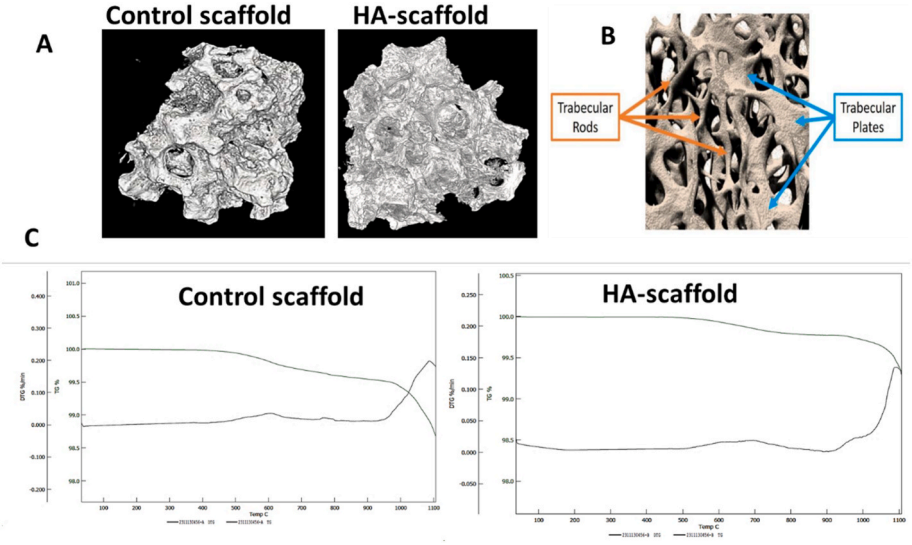

Fig. 3. Micro-CT images (A), Reference image (B) showing Rod and plate distribution in a human humeral head [41] and Thermogravimetry analysis (C) of C-Scaffold and HA-scaffold.

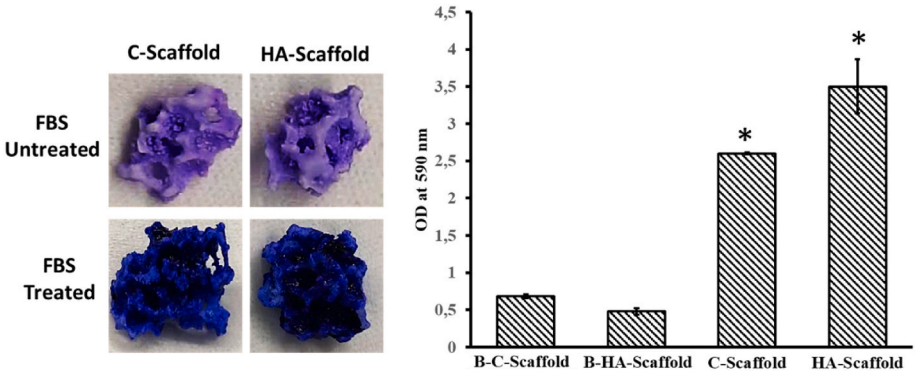

Fig. 4. The efficiency of Protein adsorption of C-Scaffold and HA-Scaffold treated with fetal bovine serum (FBS). B–C-Scaffold: Blank control scaffold (FBS untreated), B-HA-Scaffold: Blank HA-scaffold (FBS untreated), C-scaffold: control scaffold after FBS treatment, HA-scaffold: HA-scaffolds after FBS treatment. * denotes statistical significance with respective blank, $p < 0.05$.

showed, on average, total values, and a larger pore size. Total porosity was 32.4 %, distributed as 28.06 % interparticle porosity and 4.34 % intraparticle porosity. Interpore diameters varied from 172 to 6.16 μm, while intrapore diameters ranged from 0.82 to 0.034 μm. These findings are of biological significance since previous research has shown that pore sizes between 50 and 150 μm promote the exchange of nutrients and waste products through the scaffold, as well as facilitating cell colonization [32].

Furthermore, pycnometry results showed a total macroporosity, corresponding to pores >300 μM, of 86.1 ± 0.4 % in the C-Scaffold and 87.3 ± 0.6 % in the HA scaffold, relative to the total volume of the samples. These values are quite high compared to other ceramic scaffolds [33–35]. In addition, a higher rate of angiogenesis has been demonstrated to be directly related to the high scaffold macroporosity [36]. These data were complemented by the results of the compression test. The mechanical behavior of both samples was very similar, showing an approximate strength of 1.57 ± 0.2 MPa for the C-Scaffold and 1.68 ± 0.17 MPa for the HA-Scaffold. The reported strength is within the range of trabecular bone as reported by Caeiro et al. [37].

3.4. Micro-CT

Micro-CT images of both the C-Scaffold and HA-Scaffold are presented in Fig. 3A. The 3D images of micro-CT results showed that both scaffolds possessed more interconnected micro- and macro-porous structures. Interestingly, in the present study, the porous structures of scaffolds exactly mimic the trabecular spacing, trabecular rods and trabecular plates of the human humeral head (Fig. 3B).

The TGA analysis investigated the thermal denaturation profile of both the C-Scaffold and HA-scaffolds (Fig. 3C). The results showed that the first derivative of the TGA curve i.e. DTG curve, which measures the rate of sample decomposition with regards to time and temperature, was decreased slowly with respect to temperature in both the C-Scaffold and HA-scaffold. The maximum percentage of DTG was obtained at 1086.56 °C for the C-Scaffold and 1092.21 °C for HA-Scaffold, respectively. Previously, the decomposition of wollastonite hydrogel composed of silicon, Sr/Se/Zn/Mg-substituted hydroxyapatite/chitosan had a maximum TGA curve at ~850 °C [38]. In another study, the degradation behavior of β-wollastonite derived from natural waste showed that the exothermic peak observed at 778 °C indicated the starting temperature for crystallization of β-wollastonite [39]. These authors further concluded that the thermal decomposition of β-wollastonite takes place in different steps, i.e. 8.4 % weight loss from room temperature to 220 °C, 5.18 % weight loss from 220 to 600 °C and 2.5 % weight loss from 600 to 750 °C were occurred due to removal of residual water, low-temperature, and high-temperature decarbonisation, respectively [39,40].

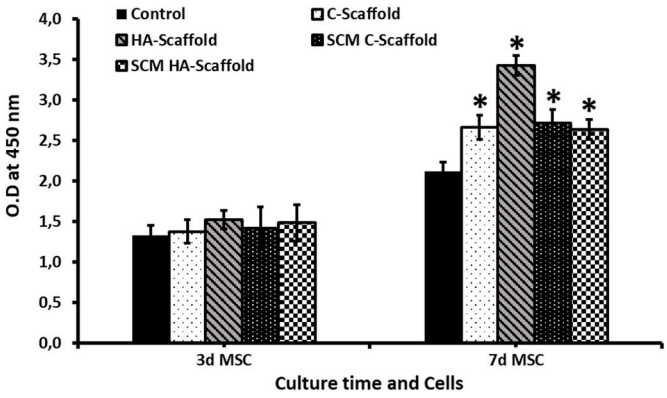

Fig. 5. The MSCs proliferative effect of C-Scaffold, HA-Scaffold and their conditioned medium (SCM). Control: cells cultured without scaffolds, C-Scaffold: cells cultured on control scaffold, HA-scaffold: cells cultured on HA-scaffold, SCM C-Scaffold: cells cultured on SCM of control scaffolds, SCM HA scaffold: cells cultured on scaffold conditioned medium of HA scaffolds. * denotes statistical significance compared to the control group (without scaffold), $P < 0.05$.

3.5. Protein adsorption

To evaluate the interaction ability of scaffolds with plasma protein receptors, scaffolds were treated with FBS and stained with CBB G-250. The protein adsorption of the C-Scaffold was about 2.6 ± 0.26 (61.2 %), which was lower than the HA-Scaffold (3.5 ± 0.11, 82.4 %), proving that the HA precipitate on the scaffold stimulated the interaction between matrix and plasma protein (Fig. 4). In addition, the blank C-Scaffold (15.9 %) and blank HA-Scaffold (11.3 %) were also partially stained with CBB G-250, even without FBS incubation, which might be due to the possible interaction of CBB G-250 dye with the active functional groups present in wollastonite and HA, respectively. Interestingly, the protein adsorption highly occurred in the interior component (inside the porous structure) of both the C-Scaffold and HA-Scaffold as evidenced by the high staining intensity of CBB G-250 observed in those regions. Our previous studies also claimed the same effect of protein adsorption in germanium-coated hydroxyapatite biomaterials and the surface coating of these materials with ethanol did not contribute to protein adsorption [23]. In the present study, the adsorption of plasma protein by scaffold was increased by HA precipitation, which was supported by earlier reports [42,43].

3.6. Effect of the scaffold on MSC proliferation

In order to investigate the cell proliferative effect of C-Scaffold and

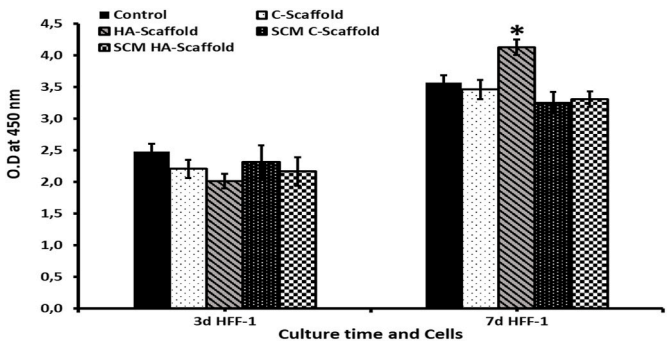

Fig. 6. The HFF-1 proliferative effect of C-Scaffold, HA-Scaffold and their conditioned medium (SCM). Control: cells cultured without scaffolds, C-Scaffold: cells cultured on control scaffold, HA-scaffold: cells cultured on HA-scaffold, SCM C-Scaffold: cells cultured on SCM of control scaffolds, SCM HA scaffold: cells cultured on scaffold conditioned medium of HA scaffolds. * denotes statistical significance compared to the control group (without scaffold), $P < 0.05$.

HA-Scaffold, the MSCs were cultured on scaffolds for 3 days and 7 days followed by the cck-8 experiment. As expected, the number of cells was higher in the 7-day culture compared to the 3-day culture in all the groups (Fig. 5). On day 3, the cell number was not altered between control cells and scaffold cultured cells, except for cells cultured on HA-Scaffold. There was not much difference between scaffold cultured cells and SCM cultured cells on 3 days of culture. On day 7, the proliferation rate of MSCs was much higher in cells cultured on HA-Scaffolds compared to control cells ($P < 0.05$) and other scaffold-cultured cells. At the same time, the cells cultured on C-Scaffold and SCM also had a higher proliferative rate than control cells ($P < 0.05$). In contrast, the cells cultured in HA-SCM did not accelerate the proliferation of MSCs compared to cells cultured on HA-scaffold and there was no significant difference in the proliferative rate of cells cultured on C-Scaffold and C-SCM on day 7.

To support the present results, many studies substantially proved the MSCs proliferative effect of wollastonite [44], wollastonite scaffold containing chitosan/carboxymethyl cellulose [45], apatite-wollastonite [46,47], apatite/wollastonite-derived porous bioactive glass-ceramic scaffolds [48], and collagen/wollastonite nanowire hybrid scaffolds [49]. Our recent data concluded that the C2S(2P6)C2S) 3D-porous scaffold coated with strontium accelerated the proliferation of mesenchymal stem cells (MSCs) [50].

3.7. Biocompatibility

The *in vitro* biocompatibility of both the C-scaffold and HA-Scaffold was investigated by culturing HFF-1 cells on both scaffolds for different periods, followed by cck-8 experiments. As shown in Fig. 6, cells cultured on day 7 had higher proliferation in C-Scaffold and scaffold-cultured cells compared to cells cultured on day 3. The cell proliferation rate of control was higher than C-Scaffold and their respective conditioned medium on day 3, however, they were not statistically significant. Interestingly, the cells cultured on HA-Scaffold had significantly higher proliferation than control and C-Scaffold or SCM cultured cells ($P < 0.05$), however, this effect was not observed in HA-SCM cultured cells.

To support the present findings, several authors investigated the biocompatibility of silk fibroin/wollastonite composite scaffolds in L929 mouse fibroblasts [51], chitosan/carboxymethyl cellulose/mesoporous wollastonite in MG-63 cells [45], wollastonite–gelatin scaffold in human mesenchymal amniotic fluid stem cells [52] and wollastonite/β-TCP in fibroblasts [53].

3.8. Effect of the scaffolds in inflammatory response

The *in vitro* biocompatibility and proliferative effect of C-Scaffold and HA-Scaffold was further confirmed by measuring cellular cytokines (IL-2 and IL-6) levels in MSCs and HFF-1 cells using ELISA experiments. On day 3, the level of IL-2 was decreased in C-Scaffold treated HFF-1 cells compared to control, however, it was not observed in HA-Scaffold treated cells. In contrast, the HA-Scaffold decreased the IL-2 level of HFF-1 cells than control and C-Scaffold cells on day 7. There were no significant changes observed in IL-2 level of MSCs between control and Scaffold cultured cells on day 3 and day 7 (Fig. 7). On the other hand, the level of IL-6 in MSCs and HFF-1 cells was not altered by either scaffold compared to their respective controls on day 3 and day 7. Recently, Kamboj et al. investigated the cytokines and anti-inflammatory factors

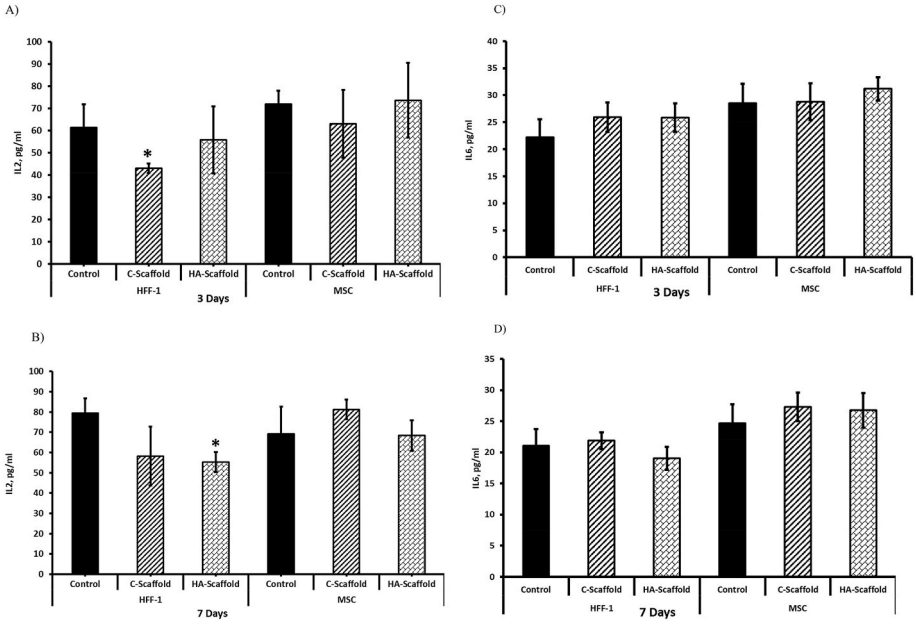

Fig. 7. The level of inflammatory cytokines (IL-2. and IL-6) in MSCs and HFF-1 cultured on C-scaffold and HA-scaffold. A-Level of IL-2 on day 3, B-Level of IL-2 on day 7, C-Level of IL-6 on day 3 and D-Level of IL-6 on day 7. Control-cells cultured without scaffolds. * denotes statistical significance compared to control, $P < 0.05$.

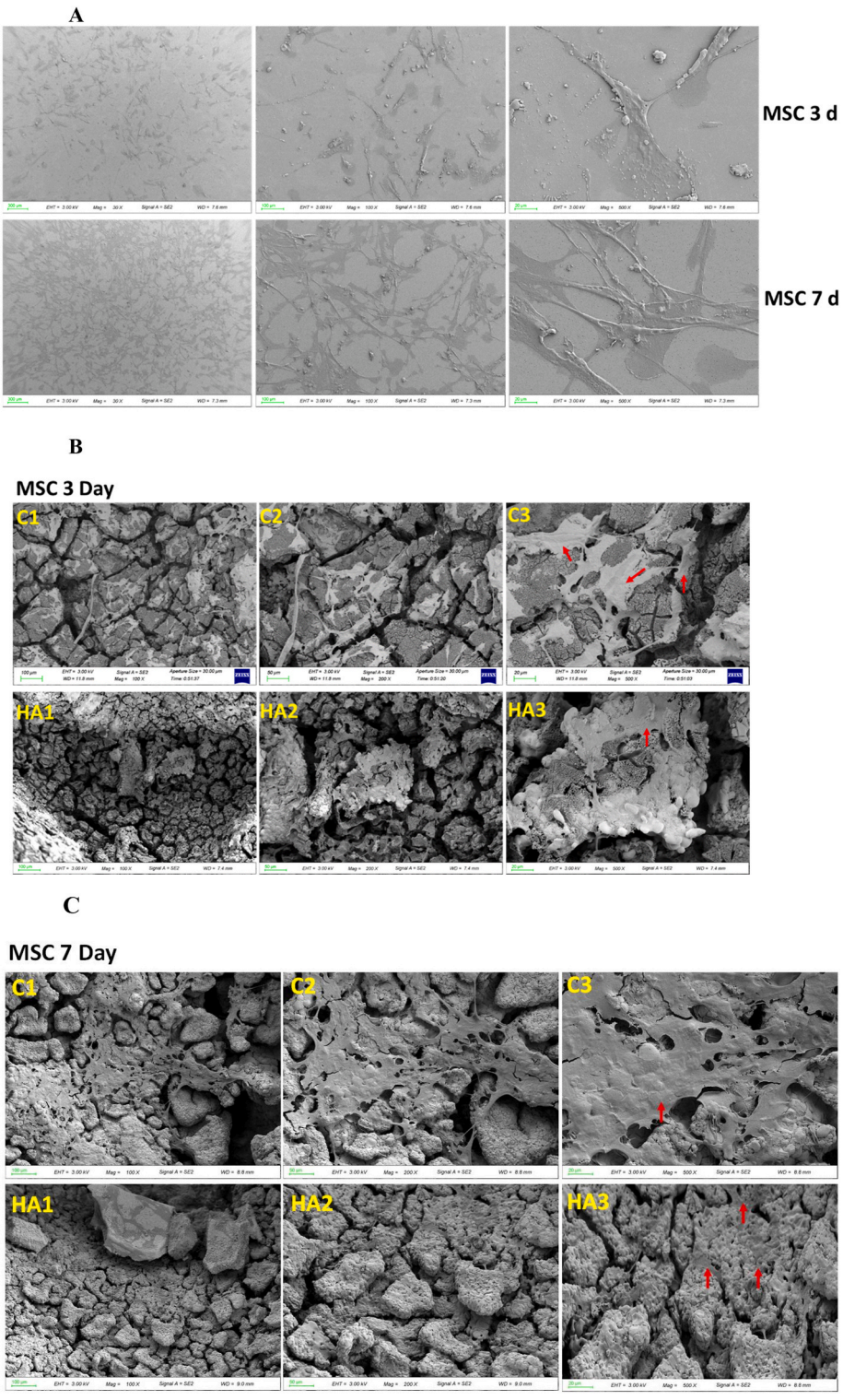

Fig. 8. Morphological structure of MSCs cultured on both C-Scaffold (C) and HA-Scaffold (HA). A- Cells without scaffolds on day 3 and day 7, B and C -Scaffolds with cells on day 3 and 7, respectively, 1, 2 and 3: images with 100, 50 and 20 μM scale bars, respectively.

of MSCs cultured on laser-sintered bio-inspired silicon-wollastonite scaffolds and concluded that the level of certain cytokines such as TGFβ, IL8, TSG6 and TGFβ was affected by the scaffolds, demonstrating possible immunomodulation effect and bone remodeling [54].

3.9. *Effect of the scaffolds on cell morphology*

The surface morphology of MSCs cultured on both C-Scaffold and HA-Scaffold is shown in Fig. 8. MSCs cultured on glass slides showed spindle and flattened shapes in both 3-day and 7-day cultures, however, the distribution of cells was increased on day 7 than on day 3 (Fig. 8A). On day 3, MSCs cultured on the C-Scaffold had a more flattened structure, whereas fibrillar cell clumps with nodules were observed in HA-Scaffold cultured cells (Fig. 8B). Fig. 8C clearly shows that on day 7 there were more cells than on day 3 and that they firmly adhered to both the control scaffold and the HA scaffolds. In the C-scaffold, the cells had

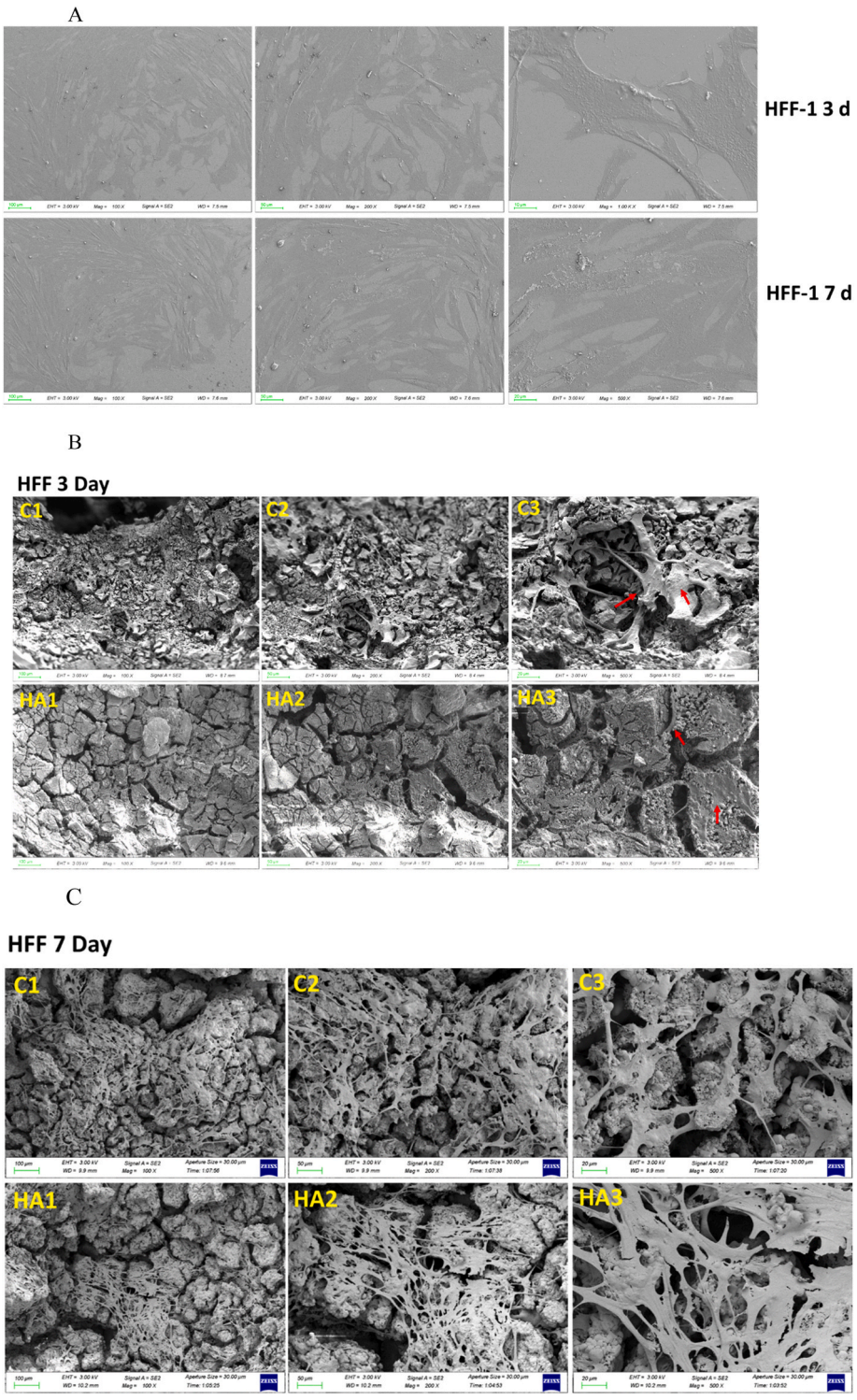

Fig. 9. Morphological structure of HFF-1 cultured on C-Scaffold (C) and HA-scaffold (HA). A- Cells without scaffolds on day 3 and day 7, B and C -Scaffolds with cells on day 3 and 7, respectively, 1, 2 and 3: images with 100, 50 and 20 μM scale bars, respectively.

a more flattened dense fibrous structure, while in the HA-scaffold cultured cells grew more in the hydroxyapatite crystal deposited region. Earlier studies reported an elongated spindle shape of MSCs cultured on apatite-wollastonite-glass ceramics for 7, 14 and 21 days [55] and long filopodia or lamellipodia shapes of Human bone marrow-derived stromal cells cultured on poly-hydroxybutyrate-*co*-hydroxyvalerate/wollastonite composite scaffolds for 7 days and 14 days [56].

Fig. 9 shows the microstructural images of HFF-1 cells cultured on scaffolds. Similar to MSCs, the HFF-1 cells were firmly grown on both the C-Scaffold and the HA-Scaffold. As observed earlier, the cell numbers were higher in 7 days culture compared to 3 days culture and more fibrillar cell structures were observed in cells cultured on C-Scaffold for 3 days than HA-Scaffold cultured cells. Compared to MSCs, the HFF-1 cells grew faster and covered all the scaffold surfaces on day 7. For instance, the surfaces of the C-Scaffold and HA-Scaffold were closely

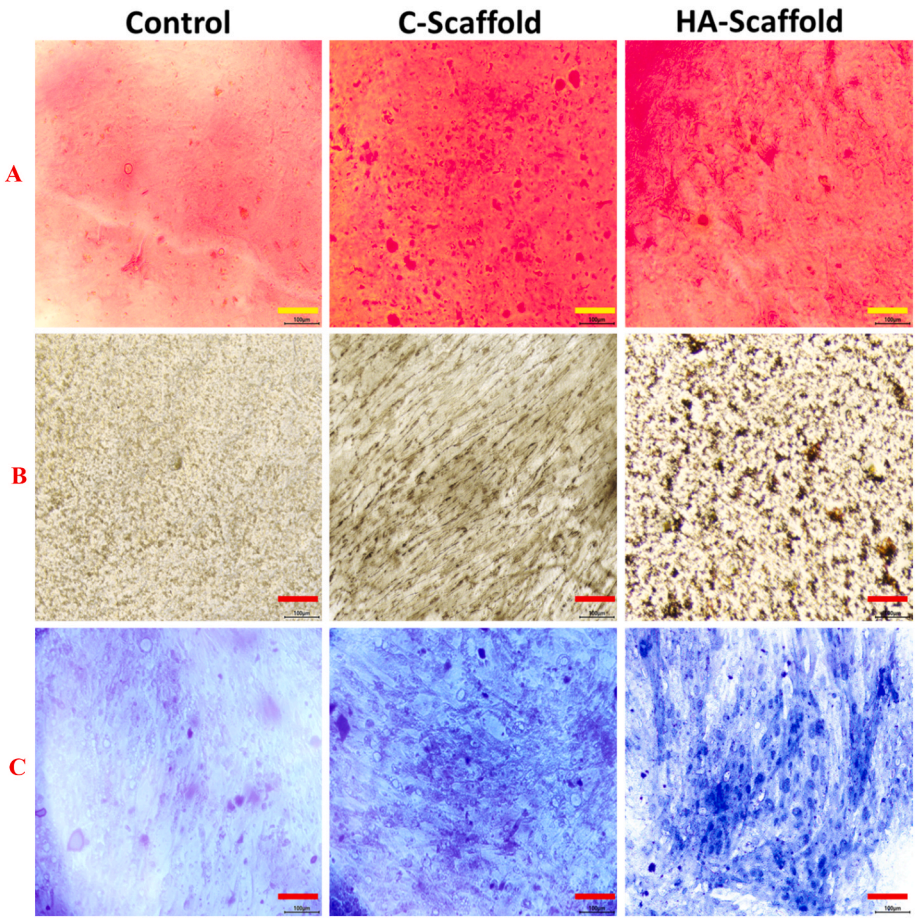

Fig. 10. Osteogenic stimulatory effect of C-Scaffold and HA-scaffold. Control-cells cultured without scaffolds, C-scaffold- cells cultured with control scaffold conditioned medium, and HA-scaffold- cells cultured with HA-scaffold condition medium. Images A- Alizarin red stain, images B- von Kossa stain and images C- Alkaline phosphatase stain. Scale bar- 100 μM.

covered by HFF-1 cells, which directly confirmed the compatibility of both scaffolds in fibroblast cell culture.

3.10. Effect of the scaffolds on cell differentiation

To test the cell regenerative ability of scaffolds, MSCs were differentiated into osteogenic cells in presence of scaffold conditioned medium. The differentiation of osteogenic cells from MSCs was confirmed by three major staining methods such as alizarin-red, von Kossa and alkaline phosphatase staining (Fig. 10). The results revealed that the control cells cultured without scaffold conditioned medium showed less staining intensity compared to those cells cultured with scaffold conditioned medium. Among the scaffold's groups, HA-scaffold conditioned medium significantly accelerated the staining intensity especially in von Kossa and alkaline phosphatase stains. Previously, Chen et al. reported that heparinised gelatine-hydroxyapatite-tricalcium phosphate scaffold enhanced the new bone regeneration and bone mineral density [57]. Similarly, Fu et al. observed the osteogenic stimulatory effect of Nano−/micro-scaled hydroxyapatite bioceramics [58]. The bone regeneration mechanism of Wollastonite and tricalcium phosphate was extensively reviewed by dos Santos et al. and concluded that the regenerative ability of these bioceramics depends on their physical-chemical, structural, functional (osteoinductivity and osteoconductivity) and biomimetic properties [59]. The present study results revealed that the osteogenic stimulatory effect of MSCs was accelerated by scaffolds, especially HA-scaffold, which directly proved the regenerative ability of this scaffolds.

4. Conclusion

The present investigation explores a novel multilayer scaffold composed of Wollastonite/$Ca_2P_6O_{17}$/TCP/Doped-Wollastonite, in which hollow hydroxyapatite spheres precipitate upon immersion in SBF. The scaffold design adheres to a structural configuration comprising a core consisting of the two innermost layers and a dual bioactive coating. Mineralogical analysis revealed that the core was predominantly composed of SiO_2 and $Ca_2P_2O_7$, possibly attributed to interlayer ionic migration. In addition, TCP and wollastonite, representing the outer bioactive layers, were also identified as predominant phases. Physical characterization of the scaffolds revealed an average overall macroporosity exceeding 85 % of their volume, along with a mechanical strength of approximately 1.6 MPa. The fabricated scaffolds resemble the trabecular spacing, trabecular rods and trabecular plates of the human humeral head. The MSCs proliferation rate was 61 % increased by HA-Scaffold compared to control cells, whereas it was 16 % in HFF cells. Interestingly, the scaffolds did not accelerate IL-2 and IL-6 cytokine levels in both MSCs and HFF cells, which further evidence the biocompatibility of these samples in tissue engineering applications. The osteogenic ability of MSCs was accelerated by HA-Scaffolds, proving their regenerative ability in stem cells. Overall, the fabricated multilayer Wollastonite/$Ca_2P_6O_{17}$/TCP/Doped-Wollastonite scaffold could be a suitable biomaterial for tissue engineering applications. However, the abilities of these materials in bone and dental cell differentiation using stem cells need to be addressed with extensive molecular signaling studies.

CRediT authorship contribution statement

Lakshmi Jeevithan: Writing – original draft, Methodology, Investigation. **Paula M. Riosalido:** Writing – original draft, Investigation. **Ángel Murciano:** Validation, Formal analysis. **Pablo Velásquez:** Visualization, Methodology. **Piedad N. De Aza:** Writing – original draft, Project administration. **Jeevithan Elango:** Writing – review & editing, Project administration. **Wenhui Wu:** Writing – review & editing, Supervision, Project administration. **Jose Eduardo Mate Sanchez de Val:** Supervision, Project administration, Funding acquisition.

Declaration of competing interest

The authors declare no conflicts of interest.

Acknowledgment

This work is part of the project PID2020-116693RB-C21 and PID2020-116693RB-C22 funded by MCIN/AEI/10.13039/501100011033 Spain. Also CIAICO/2021/157 grant funded by Generalitat Valenciana Generalitat Valenciana Spain.

Appendix A. Supplementary data

Supplementary data to this article can be found online at https://doi.org/10.1016/j.ceramint.2024.07.141.

References

[1] A. Nauth, E. Schemitsch, B. Norris, Z. Nollin, J.T. Watson, Critical-Size bone defects: is there a consensus for diagnosis and treatment? J. Orthop. Trauma 32 (2018) S7–S11, https://doi.org/10.1097/BOT.0000000000001115.
[2] J.A. Sterling, S.A. Guelcher, Biomaterial scaffolds for treating osteoporotic bone, Curr. Osteoporos. Rep. 12 (2014) 48–54, https://doi.org/10.1007/s11914-014-0187-2.
[3] H.D. Kim, S. Amirthalingam, S.L. Kim, S.S. Lee, J. Rangasamy, N.S. Hwang, Biomimetic materials and fabrication approaches for bone tissue engineering, Adv. Healthcare Mater. 6 (2017) 1700612, https://doi.org/10.1002/adhm.201700612.
[4] G. Zhu, T. Zhang, M. Chen, K. Yao, X. Huang, B. Zhang, Y. Li, J. Liu, Y. Wang, Z. Zhao, Bone physiological microenvironment and healing mechanism: basis for future bone-tissue engineering scaffolds, Bioact. Mater. 6 (2021) 4110–4140, https://doi.org/10.1016/j.bioactmat.2021.03.043.
[5] S. Bandopadhyay, N. Bandyopadhyay, S. Ahmed, V. Yadav, R.K. Tekade, Current research perspectives of orthopedic implant materials, in: Biomater. Bionanotechnol., Elsevier, 2019, pp. 337–374, https://doi.org/10.1016/B978-0-12-814427-5.00010-X.
[6] M.M. Stevens, Biomaterials for bone tissue engineering, Mater. Today 11 (2008) 18–25, https://doi.org/10.1016/S1369-7021(08)70086-5.
[7] Ž. Perić Kačarević, P. Rider, S. Alkildani, S. Retnasingh, M. Pejakić, R. Schnettler, M. Gosau, R. Smeets, O. Jung, M. Barbeck, An introduction to bone tissue engineering, Int. J. Artif. Organs 43 (2020) 69–86, https://doi.org/10.1177/0391398819876286.
[8] T.M. Koushik, C.M. Miller, E. Antunes, Bone tissue engineering scaffolds: function of multi-material hierarchically structured scaffolds, Adv. Healthcare Mater. 12 (2023) 2202766, https://doi.org/10.1002/adhm.202202766.
[9] G.J. Owens, R.K. Singh, F. Foroutan, M. Alqaysi, C.-M. Han, C. Mahapatra, H.-W. Kim, J.C. Knowles, Sol–gel based materials for biomedical applications, Prog. Mater. Sci. 77 (2016) 1–79, https://doi.org/10.1016/j.pmatsci.2015.12.001.
[10] K. Deshmukh, T. Kovářík, T. Křenek, D. Docheva, T. Stich, J. Pola, Recent advances and future perspectives of sol–gel derived porous bioactive glasses: a review, RSC Adv 10 (2020) 33782–33835, https://doi.org/10.1039/D0RA04287K.
[11] S.N.L. Ramlee, N.S.A.N. Sharifulden, H. Mohamad, S.N.F.M. Noor, Sol-gel derived bioactive glass scaffolds incorporated with polyvinyl-alcohol and pluronic P123 polymers using sponge replication technique, Mater. Today Proc. 17 (2019) 966–975, https://doi.org/10.1016/j.matpr.2019.06.463.
[12] M. González-Sánchez, C. Zamora-Ledezma, J. Elango, V. Morales-Flórez, Novel bioactive and biocompatible alumina-wollastonite porous constructs mimicking physical properties of human cortical bone, J. Eur. Ceram. Soc. 44 (2024) 4699–4708, https://doi.org/10.1016/j.jeurceramsoc.2024.02.001.
[13] C. Baudín, P. Pena, Review: tailored microstructures in the system tricalcium phosphate-wollastonite-diopside for bone regeneration scaffolds, Open Ceram 16 (2023) 100483, https://doi.org/10.1016/j.oceram.2023.100483.
[14] X. Yu, T. Zhao, Y. Qi, J. Luo, J. Fang, X. Yang, X. Liu, T. Xu, Q. Yang, Z. Gou, X. Dai, In vitro chondrocyte responses in Mg-doped wollastonite/hydrogel composite scaffolds for osteochondral interface regeneration, Sci. Rep. 8 (2018) 17911, https://doi.org/10.1038/s41598-018-36200-x.
[15] T. Shen, Y. Dai, X. Li, S. Xu, Z. Gou, C. Gao, Regeneration of the osteochondral defect by a wollastonite and macroporous fibrin biphasic scaffold, ACS Biomater. Sci. Eng. 4 (2018) 1942–1953, https://doi.org/10.1021/acsbiomaterials.7b00333.
[16] I. Tcacencu, N. Rodrigues, N. Alharbi, M. Benning, S. Toumpaniari, E. Mancuso, M. Marshall, O. Bretcanu, M. Birch, A. McCaskie, K. Dalgarno, Osseointegration of porous apatite-wollastonite and poly(lactic acid) composite structures created using 3D printing techniques, Mater. Sci. Eng. C 90 (2018) 1–7, https://doi.org/10.1016/j.msec.2018.04.022.
[17] X. Wang, M. Ye, J. Shen, J. Li, Y. Li, Z. Bao, H. Chen, T. Wu, M. Shen, C. Zhong, X. Yang, Z. Gou, S. Zhao, S. Xu, Core-shell-typed selective-area ion doping wollastonite bioceramic fibers enhancing bone regeneration and repair in situ, Appl. Mater. Today 32 (2023) 101849, https://doi.org/10.1016/j.apmt.2023.101849.
[18] P. Melo, A.-M. Ferreira, K. Waldron, T. Swift, P. Gentile, M. Magallanes, M. Marshall, K. Dalgarno, Osteoinduction of 3D printed particulate and short-fibre reinforced composites produced using PLLA and apatite-wollastonite, Compos. Sci. Technol. 184 (2019) 107834, https://doi.org/10.1016/j.compscitech.2019.107834.
[19] S. Sharma, D.J. Patil, V.P. Soni, L.B. Sarkate, G.S. Khandekar, J.R. Bellare, Bone healing performance of electrophoretically deposited apatite–wollastonite/chitosan coating on titanium implants in rabbit tibiae, J. Tissue Eng. Regen. Med. 3 (2009) 501–511, https://doi.org/10.1002/term.186.
[20] R. Sun, K. Chen, Y. Lu, Fabrication and dissolution behavior of hollow hydroxyapatite microspheres intended for controlled drug release, Mater. Res. Bull. 44 (2009) 1939–1942, https://doi.org/10.1016/j.materresbull.2009.06.015.
[21] X. Zhang, W. Zhang, Z. Yang, Z. Zhang, Nanostructured hollow spheres of hydroxyapatite: preparation and potential application in drug delivery, Front. Chem. Sci. Eng. 6 (2012) 246–252, https://doi.org/10.1007/s11705-012-1299-9.
[22] E. Sebastián, A. Murciano, P.N. De Aza, P. Velasquez, Synthesis of 3D porous ceramic scaffolds obtained by the sol-gel method with surface morphology modified by hollow spheres for bone tissue engineering applications, Ceram. Int. 49 (2023) 4393–4402, https://doi.org/10.1016/j.ceramint.2022.09.326.
[23] J. Elango, R. Bushin, A. Lijnev, P.N. De Aza, C.P.-A. Martínez, J.M.G. Marín, A. B. Hernandez, L.R.M. Olmo, J.E.M.S.D. Val, The effect of germanium-loaded hydroxyapatite biomaterials on bone marrow mesenchymal stem cells growth, Cells 11 (2022) 2993, https://doi.org/10.3390/cells11192993.
[24] J. Elango, K. Saravanakumar, S.U. Rahman, Y. Henrotin, J.M. Regenstein, W. Wu, B. Bao, Chitosan-collagen 3D matrix mimics trabecular bone and regulates RANKL-mediated paracrine cues of differentiated osteoblast and mesenchymal stem cells for bone marrow macrophage-derived osteoclastogenesis, Biomolecules 9 (2019) 173, https://doi.org/10.3390/biom9050173.
[25] N. Luo, Y. Lin, J. Guo, E. Quattrocchi, H. Deng, J. Dong, F. Ciucci, F. Boi, C. Hu, S. Grasso, Spark plasma sintering of LiFePO4: AC Field suppressing lithium migration, Materials 14 (2021) 2826, https://doi.org/10.3390/ma14112826.
[26] Y. Zhao, H. Chen, K. Ran, Y. Zhang, H. Pan, J. Shangguan, M. Tong, J. Yang, Q. Yao, H. Xu, Porous hydroxyapatite scaffold orchestrated with bioactive coatings for rapid bone repair, Biomater. Adv. 144 (2023) 213202, https://doi.org/10.1016/j.bioadv.2022.213202.
[27] M.Y. Bajuri, N. Selvanathan, F.N. Dzeidee Schaff, M.H. Abdul Suki, A.M.H. Ng, Tissue-Engineered hydroxyapatite bone scaffold impregnated with osteoprogenitor cells promotes bone regeneration in sheep model, Tissue Eng. Regen. Med. 18 (2021) 377–385, https://doi.org/10.1007/s13770-021-00343-2.
[28] X. Niu, M. Qin, M. Xu, L. Zhao, Y. Wei, Y. Hu, X. Lian, S. Chen, W. Chen, D. Huang, Coated electrospun polyamide-6/chitosan scaffold with hydroxyapatite for bone tissue engineering, Biomed. Mater. 16 (2021) 025014, https://doi.org/10.1088/1748-605X/abd68a.
[29] X. Zhou, N. Zhang, S. Mankoci, N. Sahai, Silicates in orthopedics and bone tissue engineering materials, J. Biomed. Mater. Res. 105 (2017) 2090–2102, https://doi.org/10.1002/jbm.a.36061.
[30] M. Sanmartin De Almeida, G.V.D.O. Fernandes, A.M. De Oliveira, J.M. Granjeiro, Calcium silicate as a graft material for bone fractures: a systematic review, J. Int. Med. Res. 46 (2018) 2537–2548, https://doi.org/10.1177/0300060518770940.
[31] H.R. Fernandes, A. Gaddam, A. Rebelo, D. Brazete, G.E. Stan, J.M.F. Ferreira, Bioactive glasses and glass-ceramics for healthcare applications in bone regeneration and tissue engineering, Materials 11 (2018) 2530, https://doi.org/10.3390/ma11122530.
[32] L. Zhu, D. Luo, Y. Liu, Effect of the nano/microscale structure of biomaterial scaffolds on bone regeneration, Int. J. Oral Sci. 12 (2020) 6, https://doi.org/10.1038/s41368-020-0073-y.
[33] M. Hamvar, H.R. Bakhsheshi-Rad, M. Omidi, A.F. Ismail, M. Aziz, F. Berto, X. Chen, Biocompatibility and bioactivity of hardystonite-based nanocomposite scaffold for tissue engineering applications, Biomed, Phys. Eng. Express 6 (2020) 035011, https://doi.org/10.1088/2057–1976/ab7284.
[34] J.A. Najafinezhad, M. Abdellahi, S. Nasiri-Harchegani, A. Soheily, M. Khezri, H. Ghayour, On the synthesis of nanostructured akermanite scaffolds via space holder method: the effect of the spacer size on the porosity and mechanical properties, J. Mech. Behav. Biomed. 69 (2017) 242–248, https://doi.org/10.1016/j.jmbbm.2017.01.002.
[35] A. Najafinezhad, M. Abdellahi, H. Ghayour, A. Soheily, A. Chami, A. Khandan, A comparative study on the synthesis mechanism, bioactivity and mechanical properties of three silicate bioceramics, Mater. Sci. Eng. C 72 (2017) 259–267, https://doi.org/10.1016/j.msec.2016.11.084.
[36] C.M. Walthers, A.K. Nazemi, S.L. Patel, B.M. Wu, J.C.Y. Dunn, The effect of scaffold macroporosity on angiogenesis and cell survival in tissue-engineered smooth muscle, Biomaterials 35 (2014) 5129–5137, https://doi.org/10.1016/j.biomaterials.2014.03.025.

[37] J.R. Caeiro, P. González, D. Guede, Biomecánica y hueso (y II): ensayos en los distintos niveles jerárquicos del hueso y técnicas alternativas para la determinación de la resistencia ósea, Rev. Osteoporos. Metab. Miner. 5 (2013) 99–108, https://doi.org/10.4321/S1889-836X2013000200007.
[38] A. Ressler, N. Kamboj, M. Ledinski, A. Rogina, I. Urlić, I. Hussainova, H. Ivanković, M. Ivanković, Macroporous silicon-wollastonite scaffold with Sr/Se/Zn/Mg-substituted hydroxyapatite/chitosan hydrogel, Open Ceram 12 (2022) 100306, https://doi.org/10.1016/j.oceram.2022.100306.
[39] S. Palakurthy, G.R.K. V, R.K. Samudrala, A.A. P, In vitro bioactivity and degradation behaviour of β-wollastonite derived from natural waste, Mater. Sci. Eng. C 98 (2019) 109–117, https://doi.org/10.1016/j.msec.2018.12.101.
[40] D.S. Klimesch, A. Ray, The use of DTA/TGA to study the effects of ground quartz with different surface areas in autoclaved cement: quartz pastes. Part 1: a method for evaluating DTA/TGA results, Thermochim. Acta 289 (1996) 41–54, https://doi.org/10.1016/S0040-6031(96)03033-X.
[41] G. Molino, G. Montalbano, C. Pontremoli, S. Fiorilli, C. Vitale-Brovarone, Imaging techniques for the assessment of the bone osteoporosis-induced variations with particular focus on micro-CT potential, Appl. Sci. 10 (2020) 8939, https://doi.org/10.3390/app10248939.
[42] B. Fernández-Montes Moraleda, J.S. Román, L.M. Rodríguez-Lorenzo, Influence of surface features of hydroxyapatite on the adsorption of proteins relevant to bone regeneration, J. Biomed. Mater. Res. 101A (2013) 2332–2339, https://doi.org/10.1002/jbm.a.34528.
[43] K. Chen, P. Ustriyana, F. Moore, N. Sahai, Biological response of and blood plasma protein adsorption on silver-doped hydroxyapatite, ACS Biomater. Sci. Eng. 5 (2019) 561–571, https://doi.org/10.1021/acsbiomaterials.8b00996.
[44] S. Saravanan, S. Vimalraj, M. Vairamani, N. Selvamurugan, Role of mesoporous wollastonite (calcium silicate) in mesenchymal stem cell proliferation and osteoblast differentiation: a cellular and molecular study, J. Biomed. Nanotechnol. 11 (2015) 1124–1138, https://doi.org/10.1166/jbn.2015.2057.
[45] R. Sainitya, M. Sriram, V. Kalyanaraman, S. Dhivya, S. Saravanan, M. Vairamani, T. P. Sastry, N. Selvamurugan, Scaffolds containing chitosan/carboxymethyl cellulose/mesoporous wollastonite for bone tissue engineering, Int. J. Biol. Macromol. 80 (2015) 481–488, https://doi.org/10.1016/j.ijbiomac.2015.07.016.
[46] J.A. Lee, C.A. Knight, X. Kun, X.B. Yang, D.J. Wood, K.W. Dalgarno, P.G. Genever, *In vivo* biocompatibility of custom-fabricated apatite-wollastonite-mesenchymal stromal cell constructs: custom aw-cell constructs *IN VIVO*, J. Biomed. Mater. Res. 103 (2015) 3188–3200, https://doi.org/10.1002/jbm.a.35448.
[47] S. Müller, L. Nicholson, N. Al Harbi, E. Mancuso, E. Jones, A. Dickinson, X. N. Wang, K. Dalgarno, Osteogenic potential of heterogeneous and CD271-enriched mesenchymal stromal cells cultured on apatite-wollastonite 3D scaffolds, BMC Biomed. Eng. 1 (2019) 16, https://doi.org/10.1186/s42490-019-0015-y.
[48] H. Zhang, X.-J. Ye, J.-S. Li, Preparation and biocompatibility evaluation of apatite/wollastonite-derived porous bioactive glass ceramic scaffolds, Biomed. Mater. 4 (2009) 045007, https://doi.org/10.1088/1748-6041/4/4/045007.
[49] Q. Zhang, T. Nakamoto, S. Chen, N. Kawazoe, K. Lin, J. Chang, G. Chen, Collagen/wollastonite nanowire hybrid scaffolds promoting osteogenic differentiation and angiogenic factor expression of mesenchymal stem cells, J. Nanosci. Nanotechnol. 14 (2014) 3221–3227, https://doi.org/10.1166/jnn.2014.8607.
[50] J. Elango, K. Salazar, P. Velasquez, A. Murciano, P.N. De Aza, W. Wu, J.M. Granero Marín, J.E. Mate Sanchez De Val, Fabrication of novel strontium-coated bioactive ceramic-glass (C2S(2P6)C2S) 3D-porous scaffold for the proliferation and osteogenic differentiation of bone marrow-derived mesenchymal stem cells, Ceram. Int. (2024), https://doi.org/10.1016/j.ceramint.2024.02.175. S0272884224006734.
[51] H. Zhu, J. Shen, X. Feng, H. Zhang, Y. Guo, J. Chen, Fabrication and characterization of bioactive silk fibroin/wollastonite composite scaffolds, Mater. Sci. Eng. C 30 (2010) 132–140, https://doi.org/10.1016/j.msec.2009.09.009.
[52] F. Curti, I.-C. Stancu, G. Voicu, H. Iovu, C.-I. Dobrita, L.T. Ciocan, R. Marinescu, F. Iordache, Development of 3D bioactive scaffolds through 3D printing using wollastonite–gelatin inks, Polymers 12 (2020) 2420, https://doi.org/10.3390/polym12102420.
[53] W.T. Barbosa, K.V. De Almeida, G.G. De Lima, M.A. Rodriguez, M.V. Lia Fook, R. García-Carrodeguas, V. Amaro Da Silva Junior, F.A. De Sousa Segundo, M.J. C. De Sá, Synthesis and in vivo evaluation of a scaffold containing wollastonite/β-TCP for bone repair in a rabbit tibial defect model, J. Biomed. Mater. Res. B Appl. Biomater. 108 (2020) 1107–1116, https://doi.org/10.1002/jbm.b.34462.
[54] N. Kamboj, J. Kazantseva, R. Rahmani, M.A. Rodríguez, I. Hussainova, Selective laser sintered bio-inspired silicon-wollastonite scaffolds for bone tissue engineering, Mater. Sci. Eng. C 116 (2020) 111223, https://doi.org/10.1016/j.msec.2020.111223.
[55] J.A. Dyson, P.G. Genever, K.W. Dalgarno, D.J. Wood, Development of custom-built bone scaffolds using mesenchymal stem cells and apatite-wollastonite glass-ceramics, Tissue Eng 13 (2007) 2891–2901, https://doi.org/10.1089/ten.2007.0124.
[56] H. Li, W. Zhai, J. Chang, Effects of wollastonite on proliferation and differentiation of human bone marrow-derived stromal cells in PHBV/wollastonite composite scaffolds, J. Biomater. Appl. 24 (2009) 231–246, https://doi.org/10.1177/0885328208096043.
[57] X. Chen, C.Y. Gao, X.Y. Chu, C.Y. Zheng, Y.Y. Luan, X. He, K. Yang, D.L. Zhang, VEGF-loaded heparinised gelatine-hydroxyapatite-tricalcium phosphate scaffold accelerates bone regeneration via enhancing osteogenesis-angiogenesis coupling, Front. Bioeng. Biotechnol. 10 (2022) 915181, https://doi.org/10.3389/fbioe.2022.915181.
[58] S. Fu, H. Li, Y. Wu, J. Wang, Nano−/micro-scaled hydroxyapatite ceramic construction and the regulation of immune-associated osteogenic differentiation, J. Biomed. Mater. Res. 112 (2024) 193–209, https://doi.org/10.1002/jbm.a.37606.
[59] G.G. dos Santos, L.Q. Vasconcelos, I.C. Barreto, F.B. Miguel, R.P.C. de Araújo, Wollastonite and tricalcium phosphate composites for bone regeneration, Res. Society Develop 11 (2022) e12011931662, https://doi.org/10.33448/rsd-v11i9.31662.